Supporting Information

Deprotonated Self-Assembled Molecules as Robust Hole-Selective Layers for Perovskite/Organic Tandem Solar Cells and Photocathodes

Jung Geon Son‡[a], Ha-eun Koo‡[a], Woojin Lee‡[a], Dongyoung Kim[a], Sujung Park[b], Jina Roe[a], Jongdeuk Seo[a], Jung Min Ha[c], Heunjeong Lee[b], Wangyeon Lee[a], Han Young Woo[c], Shinuk Cho[b], Dong Suk Kim*[ad], Seung-Jae Shin*[a], and Jin Young Kim*[ad]

[a] School of Energy and Chemical Engineering, Ulsan National Institute of Science and Technology (UNIST), UNIST-gil 50, Ulsan 44919, Republic of Korea

[b] Department of Semiconductor Physics and EHSRC, University of Ulsan, Ulsan 44610, Republic of Korea

[c] Department of Chemistry, Korea University, Seoul 02841, Republic of Korea

[d] Graduate School of Carbon Neutrality, Ulsan National Institute of Science and Technology (UNIST), UNIST-gil 50, Ulsan 44919, Republic of Korea

‡These authors equally contributed to this work.

Experimental Procedures

Materials

General

Formamidinium iodide (FAI, 99.99%), formamidinium bromide (FABr, 99.99%), propane-1,3-diammonium iodide ($PDAI_2$), methylammonium chloride (MACl, 99.99%), were purchased from Greatcell Solar Materials. *N,N*-Dimethylformamide (DMF, anhydrous 99.8%), dimethyl sulfoxide (DMSO, 99.9%), cesium iodide (CsI, 99.9%), cesium bromide (CsBr, 99.999%), lead chloride ($PbCl_2$, 98%), lead thiocyanate ($Pb(SCN)_2$, 99.5%), potassium thiocyanate (KSCN, 99%), molybdenum oxide (MoO_3, 99.97%), 2-propanol (IPA, anhydrous 99.5%), ethyl alcohol (EtOH, anhydrous 99.5%), chlorobenzene (CB, 99.8%), chloroform (CF, 99%), 1-chloronaphthalene (CN, 85%), potassium carbonate (K_2CO_3, 99%), potassium phosphate dibasic (K_2HPO_4, 98%), potassium phosphate monobasic (KH_2PO_4, 99%) and sodium sulfate (Na_2SO_4, 99%) were purchased from Sigma Aldrich. Lead iodide (PbI_2, 99.99%), lead bromide ($PbBr_2$, 98%), bathocuproine (BCP, 99%), and [2-(9H-Carbazol-9-yl)ethyl]phosphonic acid (2PACz, 98%) were purchased from TCI. C_{60} was purchased from Seechem. Poly[bis(4-phenyl)(2,4,6-trimethylphenyl)amine] (PTAA) was purchased from Jilin OLED. PM6, BTP-eC9 and $PC_{71}BM$ were purchased from Solarmer. Potassium perruthenate ($KRuO_4$) was purchased from SAMCHUN.

Precursor Solution Preparation

WBG perovskite precursor solution

A WBG perovskite precursor solution was prepared by dissolving 130.70 mg FAI, 49.36 mg CsI, 131.39 mg PbI_2, 244.06 mg $PbBr_2$, 0.92 mg KSCN, and 3.07 mg $Pb(SCN)_2$ with 1 ml DMF/DMSO (4:1). The precursor solution was stirred at room temperature overnight. 13.21 mg $PbCl_2$ and 3.21mg MACl were added to the precursor solution. The added solution was filtered with a 0.45 μm pore-sized PVDF filter.

NBG organic precursor solution

A narrow-bandgap organic precursor solution was prepared by dissolving PM6:BTP-eC9:$PC_{71}BM$ (weight ratio of 1:1.2:0.2, 16.8 mg ml^{-1} in total) in chloroform. 0.5 vol% of CN was added into the solution 5 min before the use of the prepared blend solution to form a BHJ organic layer.

Device Fabrication

Single-junction WBG perovskite solar cells

ITO patterned glass substrates were sequentially cleaned in deionized water, acetone, and isopropyl alcohol by ultrasonication, then dried in an oven at 80℃. The ITO substrates were subjected to UV-ozone treatment for 30 min to remove surface contaminants and improve surface wettability for uniform SAM deposition. 100 μl of 2PACz:K_2CO_3 (1:0, 1:0.5, 1:1, 1:1.5 in 1 mM in EtOH) were dropped on the substrates and spin-coated at 4000 rpm 30 s. The HSL-coated films were transferred onto a hotplate annealing at 100℃ for 10 min. The perovskite films were spin-coated at 4000 rpm for 45 s. 300 μl of CB was dropped onto the substrates at 20 s before spin-coating finished. Then, the perovskite films were treated on the hotplate at 100℃ for 30 min. Post treatment was conducted by spin-coating solution of 0.5 mg ml^{-1} $PDAI_2$ in 200:1 IPA:DMF at 4000 rpm 30 s, followed by annealing at 100℃ for 5 min. All processes were conducted in the N_2-filled glove box. Next, 15 nm of C_{60} was deposited on top of the perovskite layer by thermal evaporation (10^{-7} mbar). Then, the samples were then transferred to an ALD (Lucida D200, NCD) for deposition of the SnO_2 overlayer at a target thickness. SnO_2 was deposited at 90℃ using tetrakis(dimethylamido)tin (TDMASn) as the Sn precursor and H_2O as the oxygen precursor. One ALD cycle consisted of a 1.0 s TDMASn pulse followed by a 40 s N_2 purge, a 0.5 s H_2O pulse, and a 20 s N_2 purge. Finally, 100 nm of Ag were deposited on top of the perovskite layer by thermal evaporation (10^{-7} mbar).

Single-junction NBG organic solar cells

15 nm of MoO_3 was thermally evaporated on the prepatterned ITO. PM6:BTP-eC9:$PC_{71}BM$ were dynamically spin-coated on the MoO_3-coated ITO substrates at 3000 rpm for 30 s. A subsequent thermal annealing step at 90℃ for 5 min. Next, 10 nm of C_{60}, 5 nm of BCP, and 100 nm of Ag were deposited on top of the perovskite layer by thermal evaporation.

Perovskite/organic tandem solar cells

WBG perovskite solar cell fabrication was completed as described above until ALD process of SnO_2, after which 1 nm of Au, and 15 nm of MoO_3 were thermally deposited on the devices. PM6:BTP-eC9:$PC_{71}BM$ were dynamically spin-coated on the devices at 3000 rpm 30 s. A subsequent thermal annealing step at 90°C for 5 min. Next, 10 nm of C_{60}, 5 nm of BCP, and 100 nm of Ag were sequentially deposited on top of the perovskite layer by thermal evaporation.

Perovskite/organic tandem photocathode

10 nm of C_{60} deposited on top of the NBG organic layer by thermal evaporation. The samples were then transferred to an ALD (Lucida D200, NCD) for deposition of the TiO_x overlayer at a target thickness. TiO_x was deposited at 100°C using tetrakis(dimethylamido)titanium (TDMAT) as the Ti precursor and H_2O as the oxygen precursor. One ALD cycle consisted of a 0.5 s TDMAT pulse followed by a 40 s N_2 purge, a 0.5 s H_2O pulse, and a 30 s N_2 purge. Then, the sample edges were encapsulated by epoxy, which also defined the sample area exposed to irradiation. The RuO_2 catalyst was deposited using a photo-electrodeposition method. The device was immersed into $KRuO_4$ aqueous solution, illuminated by a solar simulator at 1 sun intensity, and subjected to 360 s of galvanostatic current density of -28 mA cm^{-2}.

Characterization

Device Characterization

Photoelectron spectroscopy

Photoelectron spectroscopy was performed in an ultra-high vacuum system, with a base pressure < 10^{-9} mbar. The UPS and XPS were conducted with ESCALAB 250XI (Thermo Fisher Scientific).

Density functional theory calculations

DFT calculations were performed using VASP (Vienna Ab initio Simulation Package) version 5.4.4 and its modified version VASPsol 5.4.4, which enables implicit solvation modeling.[S1] The projector augmented wave (PAW) method was used as implemented in the pseudopotentials. [S2] For the exchange–correlation functional, the Perdew–Burke–Ernzerhof (PBE) functional was applied, [S3] and the Hubbard U correction was introduced to account for

the self-interaction of localized *d* orbitals, where U values of 7.0 eV were applied to both indium (In) and tin (Sn) atoms. [S4,5] A kinetic energy cutoff of 520 eV was employed for the plane-wave basis set. Gaussian smearing with a width of 0.05 eV was used. [S6]

To handle the relatively large system efficiently, a Γ-centered 3×3×1 k-point grid was adopted for Brillouin zone sampling. A vacuum layer of 15 Å was added with dipole correction along the surface-normal direction to eliminate spurious electrostatic interactions due to periodic boundary conditions. Grimme's DFT-D3 (Becke–Johnson damping) correction was included to account for long-range van der Waals interactions. [S7]

The ITO slab model, composed of O, Sn, and In atoms, adopts a hexagonal phase with the lattice parameters of a = b = 14.392 Å, c = 30.017 Å. The slab consists of two layers: the bottom layer was fixed to mimic the bulk truncation, while the top layer and adsorbed molecules were fully relaxed. The convergence criterion for the self-consistent field (SCF) was set to 1×10^{-5} eV, and ionic relaxation was carried out using the conjugate gradient algorithm until the maximum force on atoms was below 0.02 eV $Å^{-1}$.

The implicit solvation model was used to simulate the screening effect that compensates for the additional negative charge introduced by the deprotonated oxygen atoms. The charge states of the singly and doubly deprotonated 2PACz molecules were set to -1 and -2, respectively. [S8]

X-ray diffraction

XRD patterns were obtained by using a high-power diffractometer (D/MAX2500V/PC, Rigaku) with settings including 40 kV potential, 200 mA current, Cu-rotating anode, Cu Kα radiation, (λ = 0.1542 nm) using a graphite monochromator and a scintillation counter.

Scanning electron microscopy (SEM) and atomic force microscopy (AFM)

SEM images were obtained with SU8220 cold FE-SEM (Hitach high-technologies). The surface morphology of the films was characterized by AFM using a Dimension ICON (Bruker Nano Surface). Samples were prepared under the optimized conditions and the measurements were conducted in the tapping mode with scan range of 24 μm × 24 μm.

Kelvin probe force microscopy (KPFM)

The CPD between the ITO and Perovskite films before and after SAM formation was measured using KPFM (SII Nano Technology Inc.).The topography and potential were

simultaneously measured using two independent lock-in amplifiers, utilizing the cantilever resonance frequency as feedback. The probe used was a Rh-coated Si cantilever with a resonance frequency of 25 kHz.

Optical characterization

UV-visible (vis) absorption spectra were obtained by using a Cary 5000 (Agilent) spectrophotometer. Excitation for the photoluminescence measurements was conducted with an nF900 instrument (Edinburgh Photonics) with a xenon lamp as an excitation source. Steady-state PL measurements were conducted using Cary Eclipse (Varian). A Xe lamp (λ = 490 nm) was used to excite the sample.

J-V and stabilized power output

J-V characteristics of solar cells were measured using a Keithley 2635A source measurement units inside the N_2-filled glove box using a high-quality optical fiber to guide the light from a solar simulator to the device under AM 1.5G irradiation at 100 mW cm^{-2}. *J-V* characteristics were measured with a scanning speed of 1 V s^{-1}. Photovoltaic parameters were extracted using an aperture area of 0.105 cm^2; the geometrical device area was 0.135 cm^2. Stabilized power output was measured by continuously tracking the current density with the voltage at the MPP under AM 1.5G irradiation.

EQE characterization

EQE measurements were conducted for the solar cells using a QEX7 system (PV Measurement, Inc.) and those of photocathode were measured using a Xe lamp (Oriel, Newport 66902) and a monochromator (Oriel, Newport 74001) operating in the wavelength range from 300 to 1000 nm controlled by a power meter (Oriel, Newport 1936-R) with a band width of 20 nm. For determination of the EQE of the tandem cells a previously published protocol was followed.[S9] The sub-cells were therefore characterized under accurate bias conditions, to emulate operation under AM 1.5G irradiation. 810 nm and 610 nm optical filters were used as bias light sources for the narrow bandgap and wide bandgap sub-cells, respectively.

Photoluminescence quantum yield (PLQY)

Absolute photoluminescence quantum yields (PLQYs) of perovskite films were determined using FP-8600 spectrofluorometer and ILF-135 integrating sphere (JASCO) with excitation

source of Xe arc lamp monochromated at 630 nm under N_2 atmosphere.

Transient photocurrent (TPC) and transient photovoltage (TPV)

TPC and transient TPV measurements were conducted using McScience T4000 at open-circuit condition and short-circuit condition, respectively, under 1 sun irradiation.

Electrical impedance spectroscopy (EIS)

EIS measurements of perovskite solar cells were conducted with a potentiostat (VMP3 and VSP-300, BioLogic) over range from 0.1 Hz to 1MHz under dark conditions. The Mott-Schottky curves were measured using a potentiostat (VMP3/VSP-300, BioLogic) in the 0 - 1.6 V voltage range and at a frequency of 0.5 MHz under dark conditions.

Linear sweep voltammetry (LSV) and chronoamperometry (CA)

LSV and CA measurements were conducted using a potentiostat (IviumStat.h) in a three-electrode system. A platinum plate was used as the counter electrode, with Ag/AgCl (with saturated KCl) electrode serving as the reference electrode. Irradiation intensity was calibrated to air mass (AM) 1.5G (100 mW cm^{-2}) using a standard silicon photodiode. LSV data were collected as a scan late of 50 mV s^{-1}, and CA data was obtained at 0.1 V_{RHE}.

Solar-to-hydrogen conversion efficiency (STH)

The solar-to-hydrogen (STH) conversion efficiency was estimated from the operating photocurrent density measured in a two-electrode configuration (photocathode–anode cell). STH efficiency is defined as the ratio of the chemical power stored in H_2 to the incident solar power:

$$STH\ (\%) = \frac{J_{op}\ \times 1.23\ V \times FE}{P_{in}}$$

Where J_{op} is the operating current density at 0 V, 1.23 V is the thermodynamic potential for overall water splitting, and FE is the Faradaic efficiency for hydrogen evolution. P_{in} is the incident power density under 1-sun illumination.

Table S1. Summary of the reported performance of perovskite-based tandem PV and PEC.

Structure	PCE (%)	STH (%)	Protection Layer	Reference
Perovskite/silicon	31.25	-	-	*Science*, 2023, 381, 59[S10]
Perovskite/silicon	33.89	-	-	*Nature*, 2024, 635, 596[S11]
Perovskite/silicon	20.9	20.8	silver/graphite	*Nat. Commun.*, 2023, 14, 3797[S12]
All-perovskite	30.6	-	-	*Nature*, 2025, 648, 600[S13]
All-perovskite	29.1	-	-	*Nat. Mater.*, 2025, 24, 252[S14]
All-perovskite	26.2	15.0	Metal foil	*ACS Energy Lett.*, 2023, 8, 2611[S15]
Perovskite/organic	26.4	-	-	*Nature*, 2024, 635, 860[S16]
Perovskite/organic	25.1	-	-	*Nat. Energy*, 2025, 10, 513[S17]
Perovskite/organic	25.1	7.7	ALD TiO_x	This work

STH values are reported only for studies in which complete tandem PEC operation was demonstrated; "-" indicates that PEC performance was not evaluated or reported in the corresponding PV-focused studies.

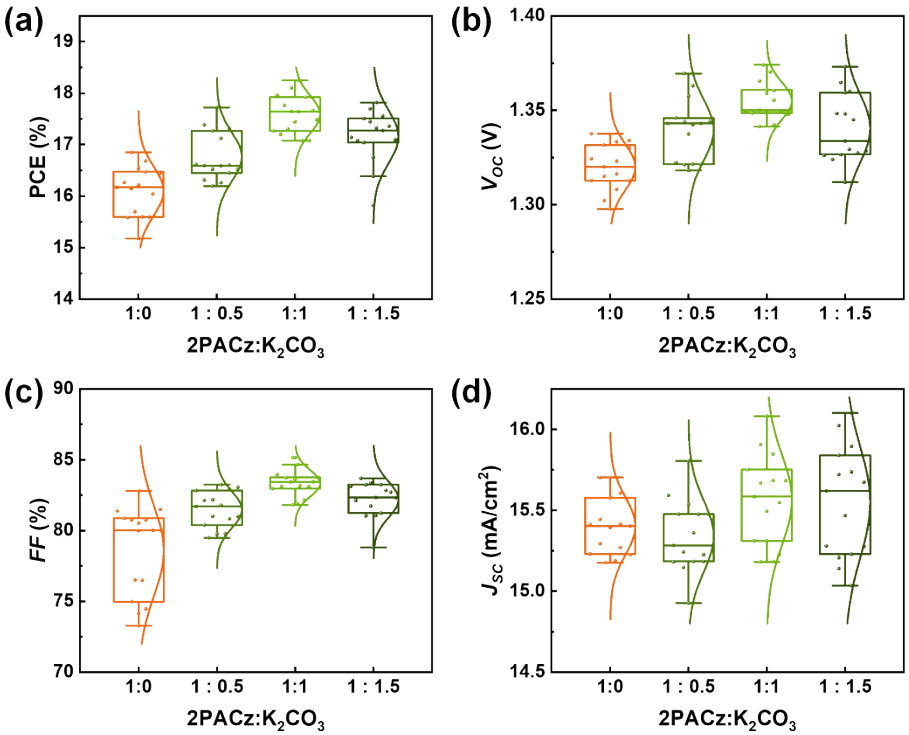

Figure S1. (a) PCE, (b) V_{OC}, (c) *FF*, and (d) J_{SC} distribution histogram of WBG PSCs with various 2PACz:K_2CO_3 ratios.

Supplementary Note 1. Calculation of deprotonation fractions of 2PACz

The deprotonation of 2PACz in ethanol was modeled using a standard diprotic acid equilibrium:

$$2PACz \rightleftharpoons 2PACz^- + H^+ \quad (p K_{a1} = \frac{[H^+][2PACz^-]}{[2PACz]})$$

$$2PACz^- \rightleftharpoons 2PACz^{2-} + H^+ \quad (p K_{a2} = \frac{[H^+][2PACz^{2-}]}{[2PACz^-]})$$

The fraction (f) of each protonation state was calculated as follows:

$$f_{2PACz} = \frac{[2PACz]}{[2PACz] + [2PACz^-] + [2PACz^{2-}]} = \frac{[H^+]^2}{[H^+]^2 + K_{a1}[H^+] + K_{a1}}$$

$$f_{2PACz^-} = \frac{[2PACz^-]}{[2PACz] + [2PACz^-] + [2PACz^{2-}]} = \frac{K_{a1}[H^+]}{[H^+]^2 + K_{a1}[H^+] + K_{a1}}$$

$$f_{2PACz^{2-}} = \frac{[2PACz^{2-}]}{[2PACz] + [2PACz^-] + [2PACz^{2-}]} = \frac{K_{a1}K_{a2}}{[H^+]^2 + K_{a1}[H^+] + K_{a1}}$$

where f_{2PACz}, f_{2PACz^-}, $f_{2PACz^{2-}}$ denote the fractions of the fully protonated, mono-deprotonated, and di-deprotonated species, respectively.

Table S2. Calculated distribution of protonation states (2PACz, 2PACz$^-$, and 2PACz^{2-}) and corresponding P-OH:P-O$^-$ ratios for 2PACz and 2PACz:K_2CO_3 (1:1) in ethanolic solution.

Condition	2PACz (%)	2PACz$^-$ (%)	2PACz^{2-} (%)	P-OH : P-O$^-$
2PACz	29.42	70.58	1.69×10^{-4}	0.65:0.35
2PACz:K_2CO_3 (1:1)	1.55×10^{-4}	69.12	30.88	0.35:0.65

Table S3. Relative peak areas of P=O, P-OH, and P-O$^-$ from O 1*s* XPS spectra of 2PACz and 2PACz-K films on glass.

Condition	P=O Peak Area	P-OH Peak Area	P-O$^-$ Peak Area	P-O:P-O$^-$
2PACz	30537	41555	23878	0.64:0.36
2PACz-K	51240	24424	77235	0.24:0.76

Supplementary Note 2. Calculation of adsorption energy (E_{ads})

The E_{ads} of HSLs on the ITO surface were calculated using the following equation[S18]:

$$E_{ads} = E_{total} - (E_{HSL} + E_{In_2O_3})$$

where E_{total} is the total energy of the HSL/ITO adsorption system, E_{HSL} is the total energy of the isolated HSL molecule (2PACz, $2PACz^-$, and $2PACz^{2-}$), and $E_{In_2O_3}$ is the total energy of bare ITO. A more negative E_{ads} value indicates a stronger adsorption affinity of the HSL molecules to the ITO surface.

Table S4. CPD values and corresponding FWHM extracted from KPFM images of bare ITO, ITO/2PACz, and ITO/2PACz-K.

Condition	CPD (V)	FWHM (mV)
Bare ITO	1.00	2.86
2PACz before rinsing	0.86	2.31
2PACz after rinsing	0.97	3.97
2PACz-K before rinsing	0.85	1.50
2PACz-K after rinsing	0.91	2.48

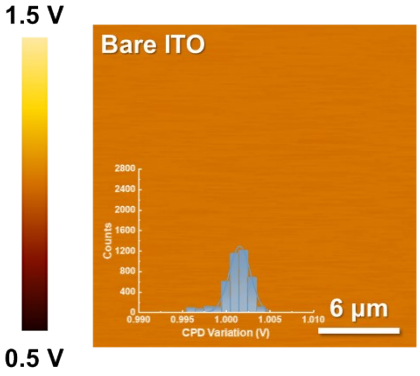

Figure S2. KPFM image and corresponding Gaussian fitting curve of CPD for bare ITO.

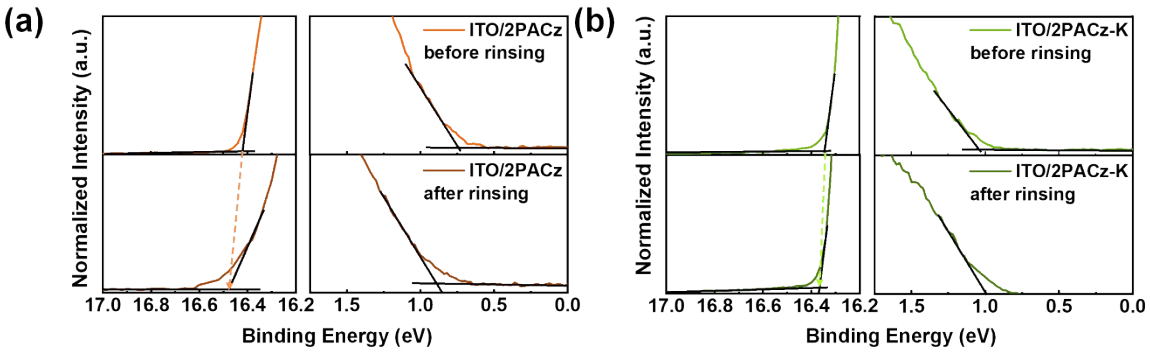

Figure S3. UPS spectra of the (a) ITO/2PACz and (b) ITO/2PACz-K.

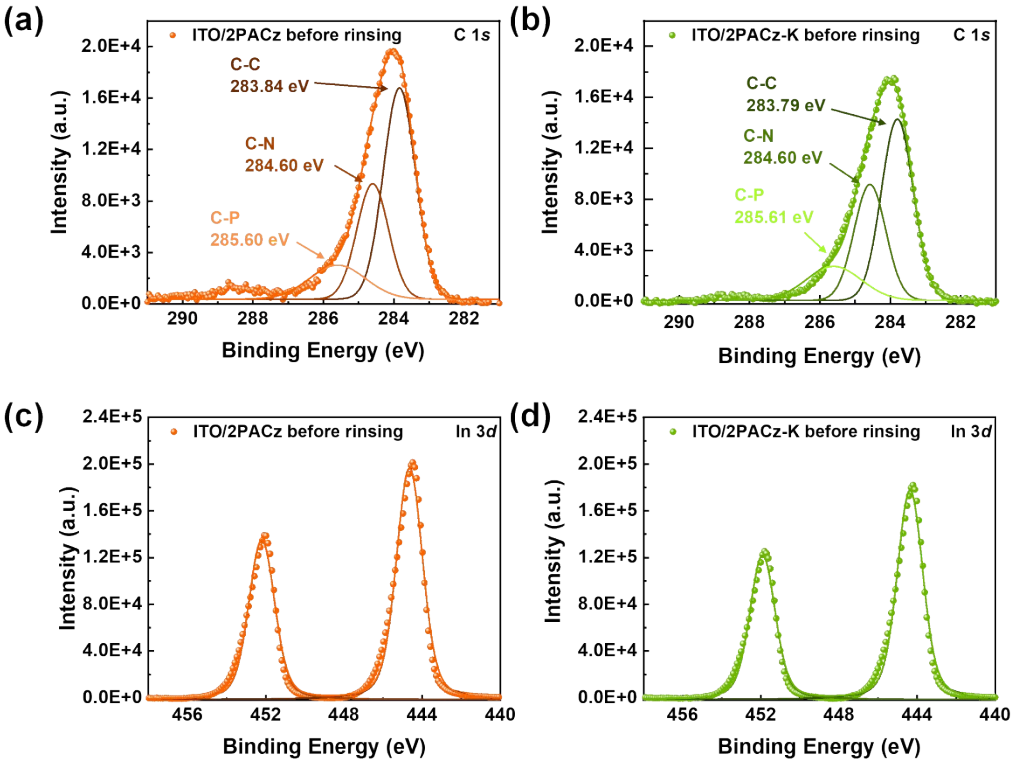

Figure S4. XPS spectra of ITO/HSLs before DMF rinsing: (a-b) C 1*s* and (c-d) In 3*d* core-level spectra.

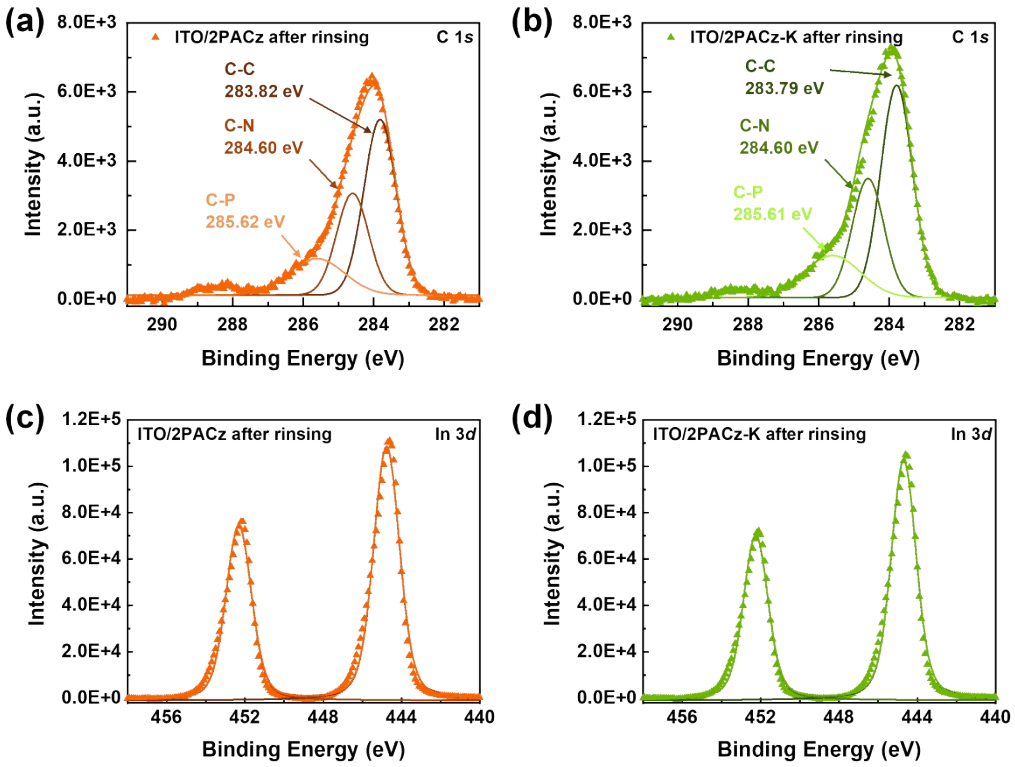

Figure S5. XPS spectra of ITO/HSLs after DMF rinsing: (a-b) C 1*s* and (c-d) In 3*d* core-level spectra.

Table S5. Coverage factors calculated from C 1*s* and In 3*d* XPS spectra, along with corresponding fitting parameters, for ITO/HSLs before and after DMF rinsing.

Condition	C 1*s* Area	In $3d_{5/2}$ Area	Carbon Atoms	Coverage factor (10^{-3})
2PACz before rinsing	34254	380630	14	6.43
2PACz after rinsing	11268	209060	14	3.85
2PACz-K before rinsing	31670	334333	14	6.77
2PACz-K after rinsing	13230	191927	14	4.92

$$coverage\ factor = \frac{C\ 1s\ area}{\#\ of\ C\ atoms \times In\ 3d_{5/2}\ area}$$

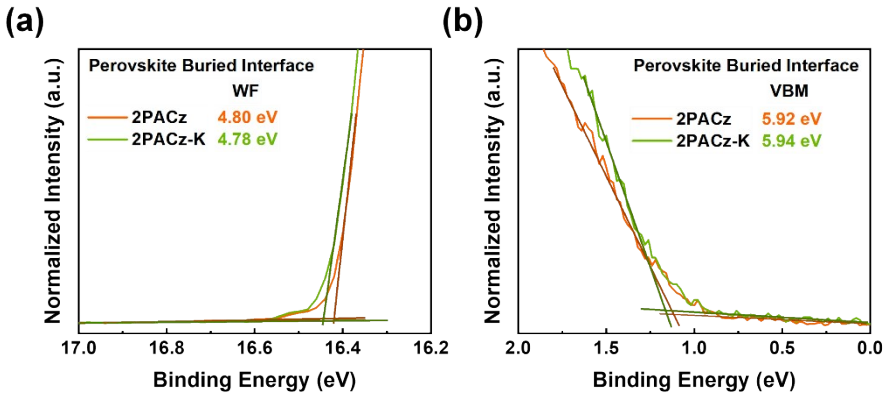

Figure S6. UPS spectra in the (a) high binding energy region and (b) low binding energy region of perovskite buried interfaces on ITO/HSLs.

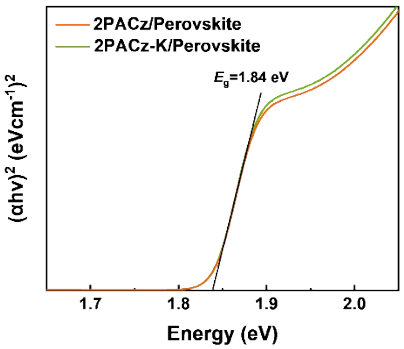

Figure S7. Tauc plots for the perovskite films on ITO/HSLs.

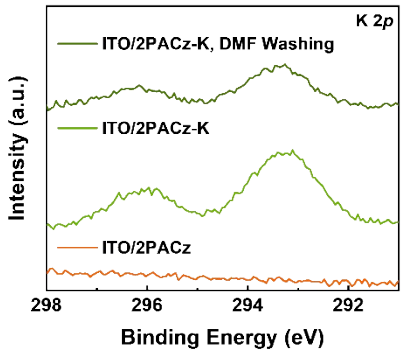

Figure S8. K 2*p* XPS spectra of ITO/HSLs before and after rinsing with DMF.

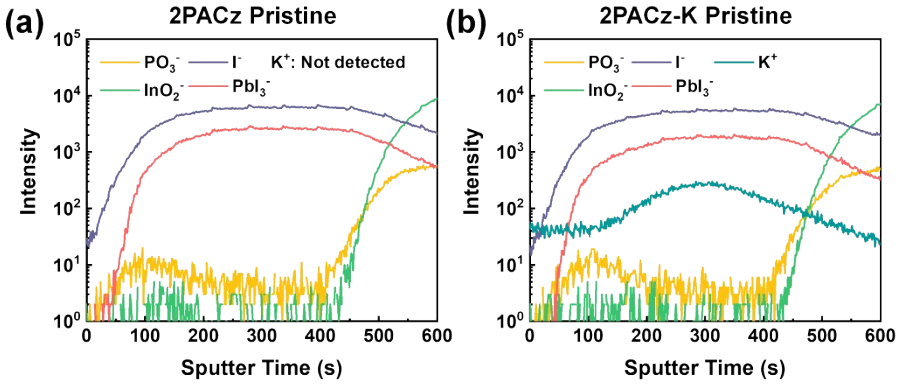

Figure S9. TOF-SIMS depth profiles of (a) ITO/2PACz/perovskite, (b) ITO/2PACz-K/perovskite structures in the as-prepared state.

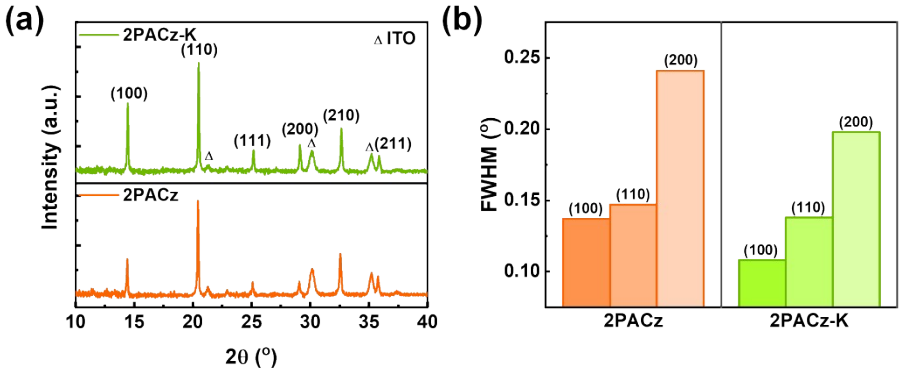

Figure S10. (a) XRD patterns of perovskite films on ITO/HSLs. (b) FWHM of (100), (110), and (200) planes of perovskite films on ITO/HSLs.

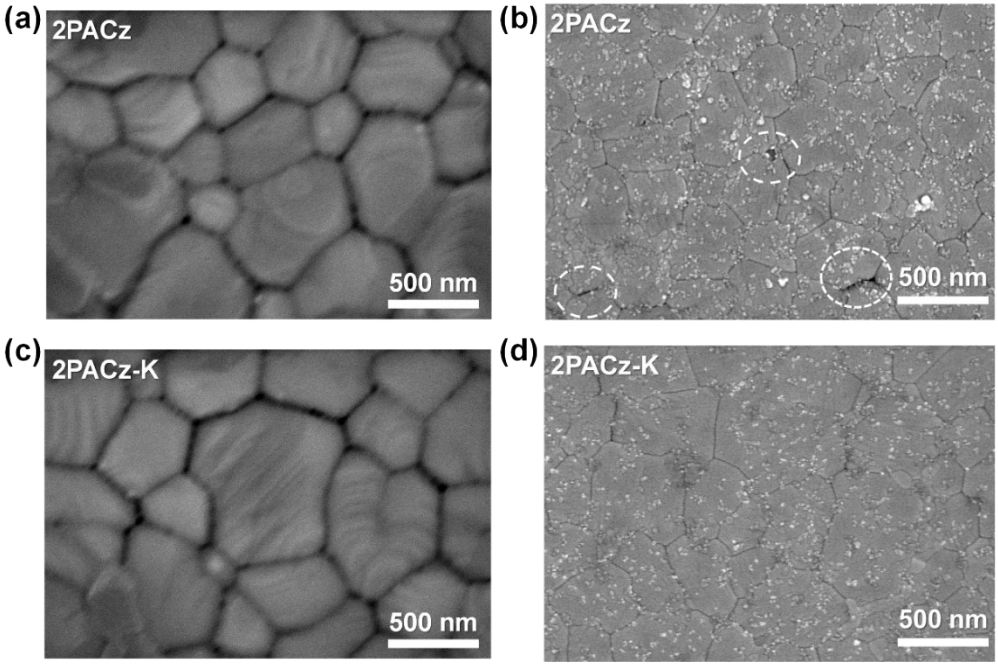

Figure S11. SEM images of perovskite films on ITO/HSLs: (a,c) top surface and (b,d) buried interface.

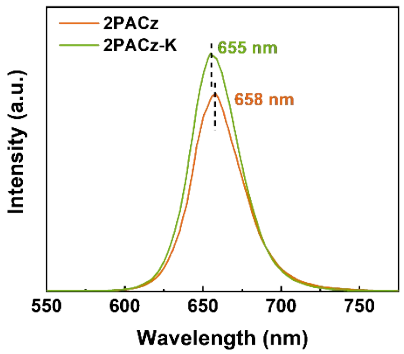

Figure S12. PL spectra of perovskite films on ITO/HSLs.

Supplementary Note 3. Calculation of residual stress (σ)

The GIXRD was conducted for evaluating the residual strain in the perovskite, the peak position of the (210) plane was recorded continuously by increasing the tilt angle ψ from 5 to 45 °. with increasing tilt angle, the (210) peaks gradually shifted to smaller 2θ for the perovskite films on ITO/HSL. This implies an increase in the crystal plane distance ($d_{(210)}$) and tensile strain in the perovskite films.[S19,20]

The residual stress (σ) was calculated using the following equation:

$$\sigma = -\frac{E}{2(1+\nu)}\frac{\pi}{180^o}cot\theta_0\frac{\partial(2\theta)}{\partial(\sin^2\psi)}$$

where E, ν, and $2\theta_0$ denote the perovskite modulus, the Poisson ratio, and the diffraction angle corresponding to the given diffraction peak for stress-free perovskite, respectively. [S19]

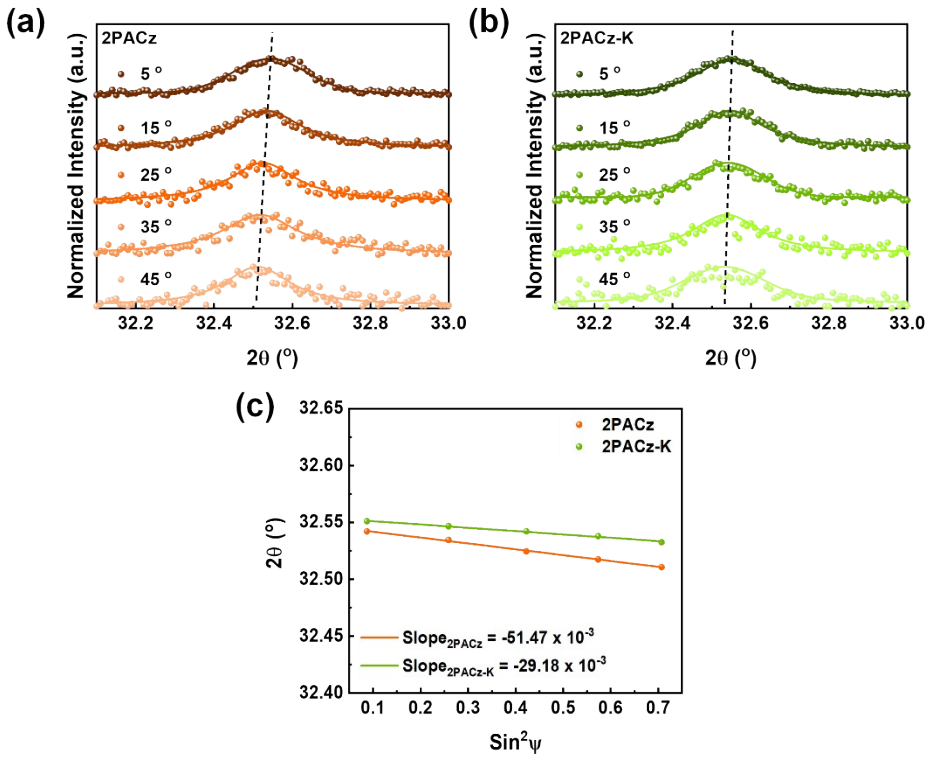

Figure S13. GIXRD patterns at different tilt angles for perovskite films on (a) ITO/2PACz and (b) ITO/2PAC-K. (c) Residual strain distribution for perovskite films on ITO/HSLs.

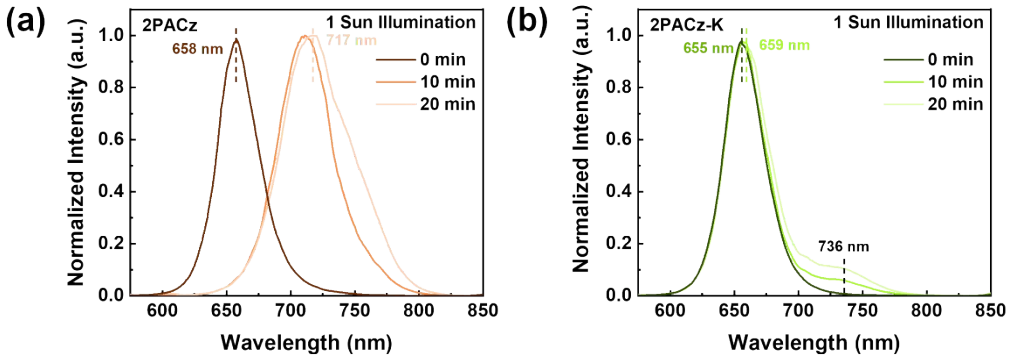

Figure S14. Time-dependent PL spectra for perovskite films on (a) ITO/2PACz and (b) ITO/2PACz-K.

Table S6. Photovoltaic parameters and hysteresis index of WBG PSCs with 2PACz and 2PACz-K.

Condition	Scan Direction	J_{SC} (mA cm^{-2})	V_{OC} (V)	*FF* (%)	PCE (%)	Hysteresis Index
2PACz	Reverse	15.70	1.319	80.54	16.54	0.0701
	Forward	15.59	1.323	74.59	15.38	
2PACz-K	Reverse	16.08	1.366	83.10	18.25	0.0466
	Forward	15.95	1.343	81.27	17.40	

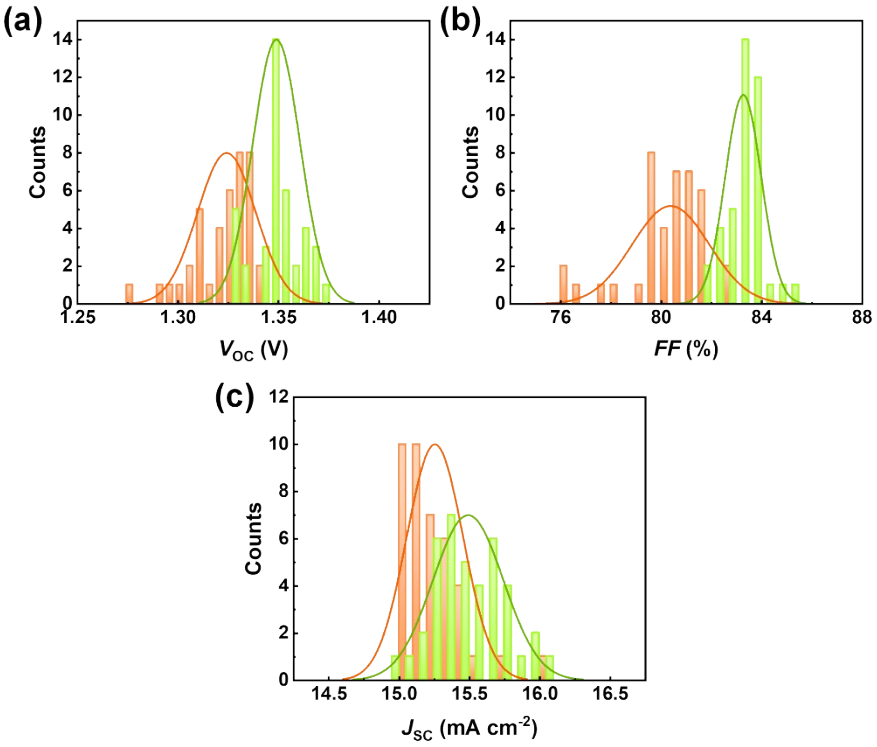

Figure S15. (a) V_{OC}, (b) *FF*, and (c) J_{SC} distribution histogram of WBG PSCs with 2PACz and 2PACz-K.

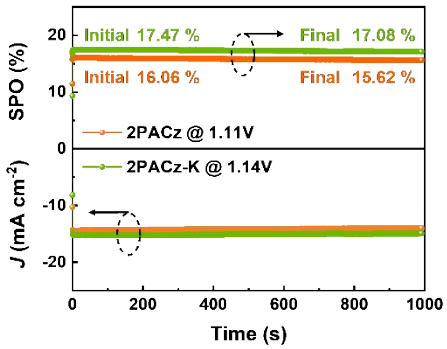

Figure S16. SPO tracking of WBG PSCs with 2PACz and 2PACz-K.

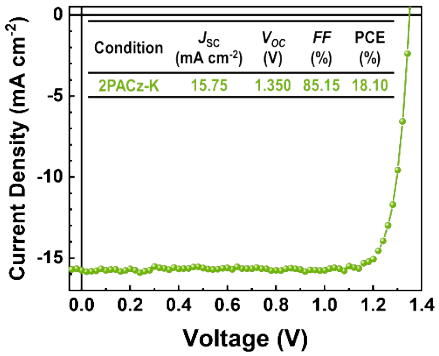

Figure S17. *J-V* curve for WBG PSCs with 2PACz-K of the highest *FF*.

Table S7. Summary of the reported V_{OC} and *FF* values of WBG PSCs.
(*Aperture and/or geometrical device active areas are additionally listed where explicitly reported.*).

E_g (eV)	V_{oc} (V)	*FF* (%)	V_{OC} × *FF* (V)	Aperture Area / Device Active Area	Reference
1.84	1.366	83.10	1.135	0.105 cm^2 / 0.135 cm^2	This work
	1.350	85.15	1.150		
1.86	1.366	84.2	1.15	0.055 cm^2 / NA	*Joule*, 2024, 8, 2554[S21]
1.85	1.361	83.34	1.134	NA / 0.040 cm^2	*Nat. Commun.*, 2025, 16, 2759[S22]
1.91	1.305	86.87	1.134	NA / 0.040 cm^2	*Energy Environ. Sci.*, 2024, 17, 219[S23]
1.85	1.36	83.21	1.132	NA / 0.0324 cm^2	*Adv. Mater.*, 2023, 36, 2306568[S24]
1.85	1.35	83.29	1.124	0.034 cm^2 / NA	*Adv. Mater.*, 2023, 35, 2305946[S25]
1.85	1.37	81.81	1.121	0.1 cm^2 / NA	*J. Mater. Chem. C*, 2025, 13, 6309[S26]
1.84	1.366	81.88	1.118	NA / NA	*Adv. Energy Mater.*, 2025, 2404092[S20]

E_g (eV)	V_{OC} (V)	*FF* (%)	V_{OC} *FF* (V)	Aperture Area / Device Active Area	Reference
1.81	1.351	82.74	1.118	0.0644 cm^2 / NA	*Nat. Energy*, 2024, 9, 411[S27]
1.84	1.32	84.21	1.112	0.0628 cm^2 / NA	*Nat. Energy*, 2024, 9, 592[S28]
1.91	1.36	81.43	1.107	0.062 cm^2 / 0.0988 cm^2	*Adv. Mater.*, 2023, 35, 2208604[S29]
1.85	1.34	81	1.085	0.0174 cm^2 / 0.0314 cm^2	*Nature*, 2022, 604, 280[S9]
1.9	1.3	82.98	1.079	NA / NA	*Energy Environ. Sci.*, 2025, 18, 2536[S30]
1.77	1.33	80.94	1.077	0.1 cm^2 / NA	*Adv. Funct. Mater.*, 2023, 33, 2308794[S31]
1.9	1.269	84.79	1.076	0.04 cm^2 / NA	*Nano Energy*, 2020, 78, 105238[S32]
1.79	1.25	83	1.038	0.0625 cm^2 / NA	*Adv. Mater.*, 2022, 34, 2108829[S33]
1.77	1.24	81.44	1.01	NA / NA	*Adv. Mater.*, 2023, 35, 2307502[S34]
1.79	1.26	78.9	0.994	0.08 cm^2 / 0.1425 cm^2	*Nat. Energy*, 2022, 7, 229[S35]
1.93	1.25	75.85	0.948	NA / 0.0988 cm^2	*Adv. Funct. Mater.*, 2021, 32, 2109321[S36]
1.79	1.15	81.19	0.934	NA / NA	*J. Mater. Chem. A*, 2021, 9, 19778[S37]
1.72	1.19	78.4	0.933	NA / NA	*Adv. Funct. Mater.*, 2022, 32, 2112126[S38]
1.77	1.113	82.4	0.917	0.062 cm^2 / NA	*Joule*, 2020, 4, 1594[S39]
1.7	1.21	75.12	0.909	NA / 0.13 cm^2	*Adv. Energy Mater.*, 2020, 10, 2000361[S40]

E_g (eV)	V_{OC} (V)	*FF* (%)	V_{OC} *FF* (V)	Aperture Area / Device Active Area	Reference
1.85	1.15	77.72	0.894	0.0518 / NA	*Adv. Energy Mater.*, 2020, 10, 2001188[S41]

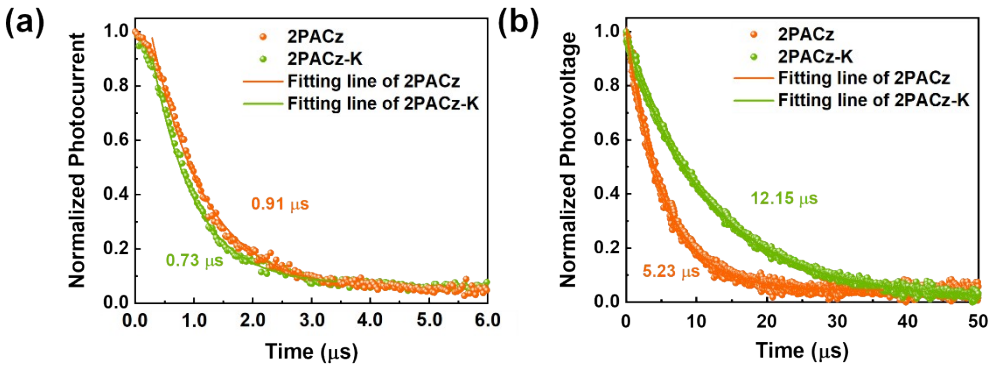

Figure S18. (a) TPC and (b) TPV measurements of WBG PSCs with 2PACz and 2PACz-K.

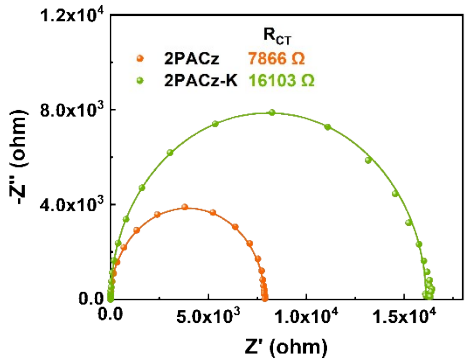

Figure S19. Nyquist plots of WBG PSCs with 2PACz and 2PACz-K.

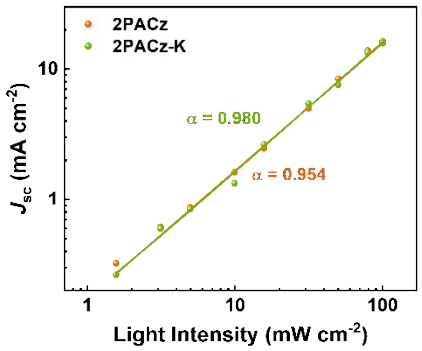

Figure S20. J_{SC} vs light intensity dependence of the WBG PSCs with 2PACz and 2PACz-K.

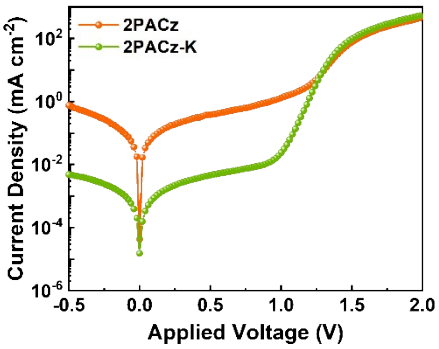

Figure S21. Dark *J-V* characteristics of WBG PSCs employing 2PACz and 2PACz-K measured under dark conditions.

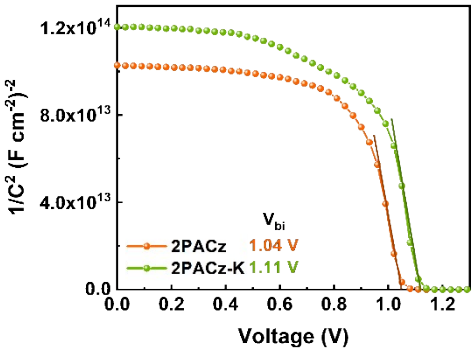

Figure S22. Mott-Schottky plots of WBG PSCs with 2PACz and 2PACz-K.

Supplementary Note 4. Calculation of QFLS

$\phi_{BB}(E)$ is the black-body photon flux, which can be determined by the following equation:

$$\phi_{BB}(E) = \frac{2\pi E^2}{(h^3c^2)} exp(\frac{-E}{k_B T})$$

where E is the photon energy h is the Plank constant, c is the light velocity in vacuum, k_B is the Boltzmann constant, and T is the temperature. Assuming that the perovskite cell is at 300K in thermal equilibrium with its environment, the dark radiative saturation current density ($J_{rad,0}$) can be calculated by the following equation:

$$J_{rad,0} = q \int EQE_{PV}(E)\phi_{BB}(E)dE$$

where q is the elementary charge and $EQE_{PV}(E)$ is the photovoltaic external quantum efficiency of the perovskite solar cell. From that, the radiative limit of the QFLS ($QFLS_{rad}$) can be obtained from the following equation:

$$QFLS_{rad} = k_B T ln(\frac{J_G}{J_{rad,0}})$$

where J_G is the integral product of the EQE spectrum.

Internal QFLS can be determined based on the relationship between PLQY according to the following equation:

$$QFLS = QFLS_{rad} + k_B T ln(PLQY)$$

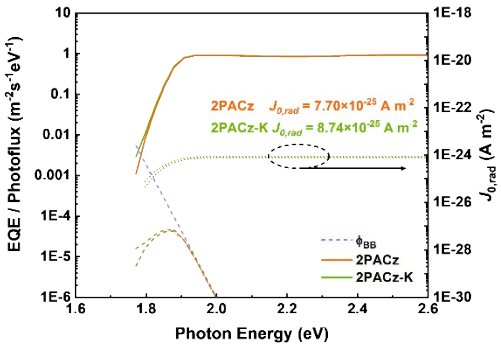

Figure S23. EQE_{PV} onset (black and red line) convoluted with the black-body (ϕ_{BB}) radiation

of the surroundings at 300K (purple dashed line).

The perovskite emission spectra resulting from the convolution is plotted in black and red dashed lines. The latter emission spectra are integrated over the photon energy and multiplied by the elementary charge q in order to calculate the dark radiative current $J_{0,\,rad}$, plotted in black and red dotted lines.

Table S8. Photophysical parameters for perovskite films on ITO/HSLs.

Condition	J_G (mA cm^{-2})	$J_{rad,0}$ (A m^{-2})	$QFLS_{rad}$ (eV)	PLQY (%)	QFLS (eV)	V_{OC} (V)	$\Delta V_{non\text{-}rad}$ (mV)	ΔV_{int} (mV)
2PACz	15.67	7.70×10^{-25}	1.509	0.896	1.385	1.319	124	66
2PACz-K	15.87	8.74×10^{-25}	1.506	2.932	1.412	1.366	94	46

The non-radiative recombination voltage loss ($\Delta V_{non\text{-}rad}$) and interfacial voltage loss (ΔV_{int}) were defined as:

$$\Delta V_{non\text{-}rad} = QFLS_{rad} - QFLS$$

$$\Delta V_{int} = QFLS - V_{OC}$$

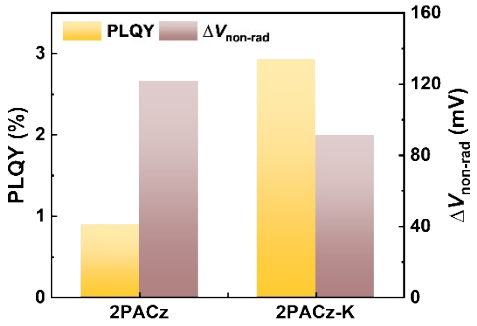

Figure S24. PLQY and corresponding non-radiative voltage loss ($\Delta V_{non\text{-}rad}$) of perovskite films on ITO/HSLs.

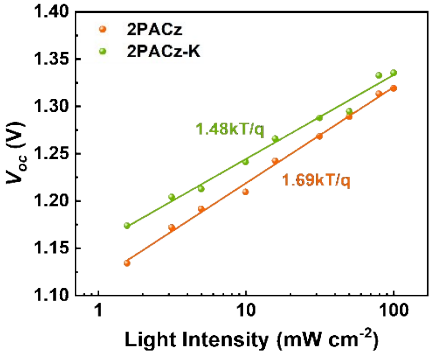

Figure S25. V_{OC} vs light intensity dependence of the WBG PSCs with 2PACz and 2PACz-K.

Supplementary Note 5. Calculation of FF_{max} and transport loss

The maximum *FF* (FF_{max}) in the absence of charge transport loss can be calculated using the following equation and the extracted ideality factor:[S20]

$$FF_{max} = \frac{v_{oc} - ln(v_{oc} + 0.72)}{v_{oc} + 1} \quad \text{(where } v_{oc} = \frac{qV_{OC}}{nkT}\text{)}$$

The transport loss was then quantified as the difference between FF_{max} and the experimentally measured FF extracted from the *J*-*V* characteristics:

$$\text{Transport loss} = FF_{max} - FF$$

This approach allows the FF loss originating from the charge transport and extraction limitations to be distinguished from non-radiative recombination loss.

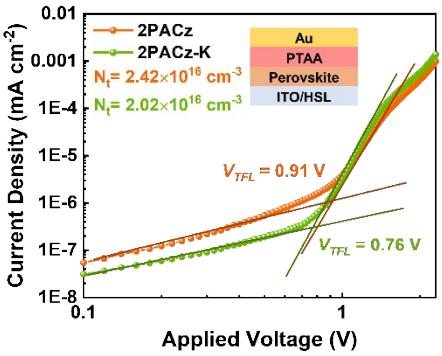

Figure S26. SCLC measurements of the hole-only devices with 2PACz and 2PACz-K (the inset showing the device structures).

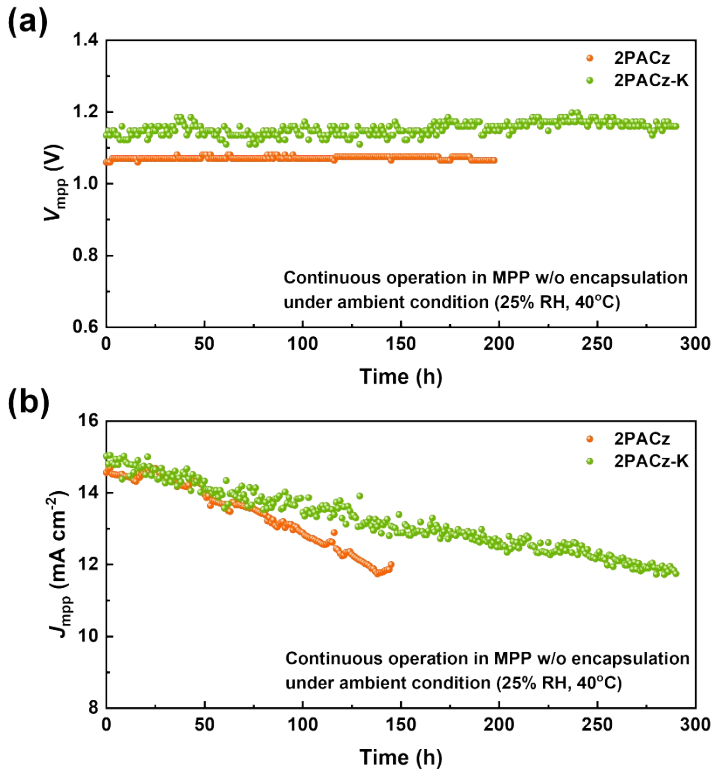

Figure S27. Operation stability of WBG PSCs with 2PACz and 2PACz-K at continuous output at MPP in ambient condition (25% RH, 40°C) under 100 mW cm^{-2}. (a) V_{mpp} and (b) J_{mpp}, respectively.

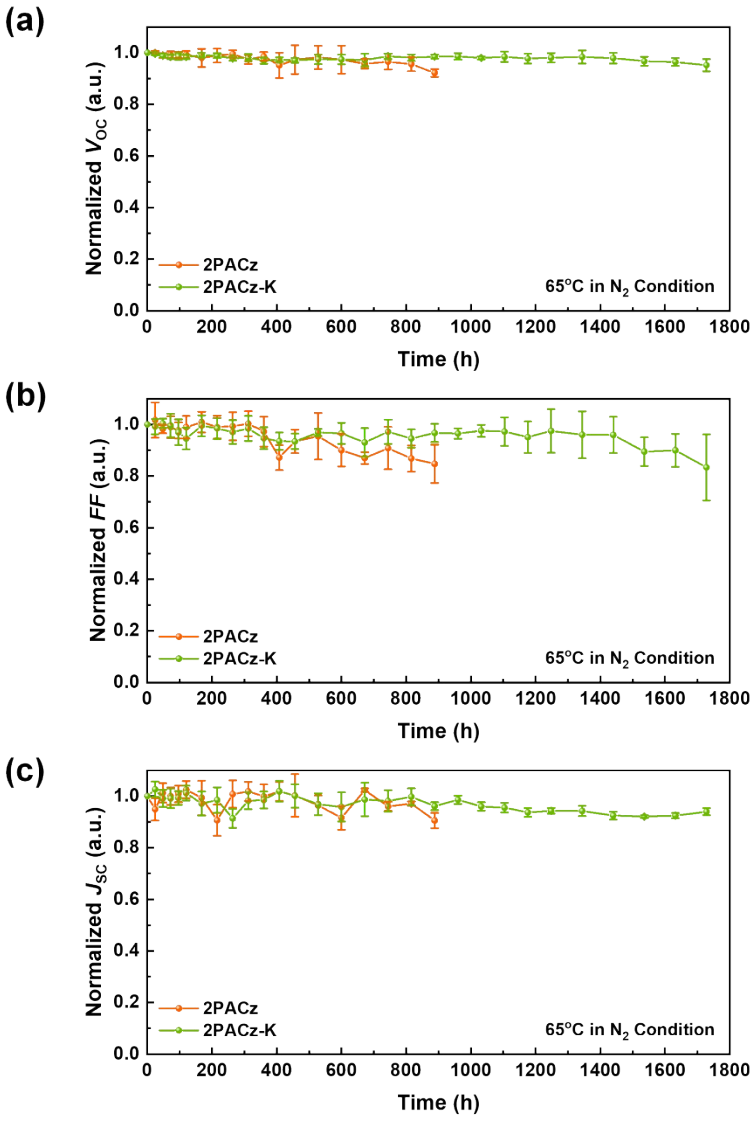

Figure S28. Thermal stability of WBG PSCs with 2PACz and 2PACz-K under 65℃ in N_2 atmosphere. Normalized (a) V_{OC}, (b) *FF*, and (c) J_{SC}, respectively.

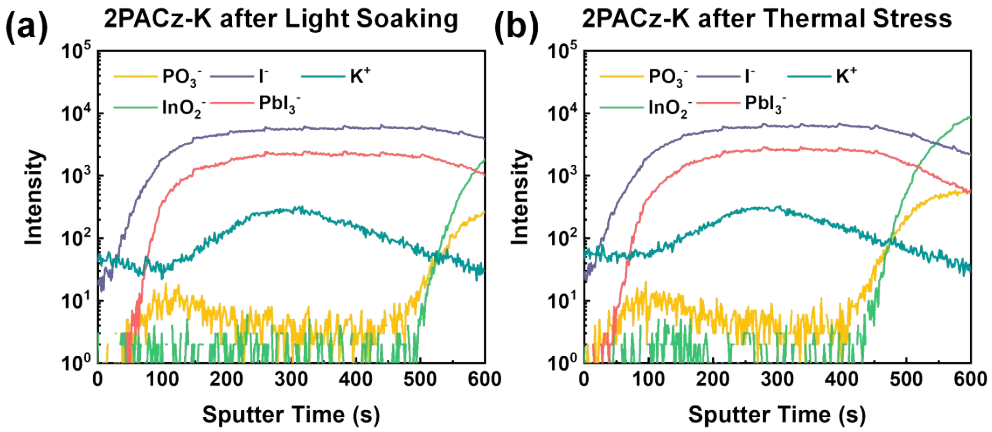

Figure S29. TOF-SIMS depth profiles of ITO/2PACz-K/perovskite (a) after light soaking for 100 h and (b) after thermal stress for 100 h.

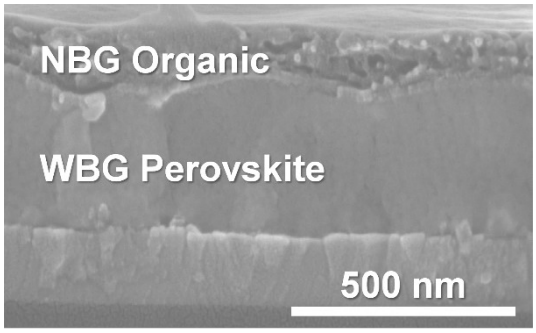

Figure S30. Cross-sectional SEM images of POTSCs.

Table S9. Photovoltaic parameters of champion perovskite-sub cell, organic sub-cell, and POTSCs.

Condition	J_{sc} (mA cm^{-2})	V_{oc} (V)	*FF* (%)	PCE (%)
Perovskite Sub-cell	16.08	1.366	83.10	18.25
Organic Sub-cell	26.91	0.873	69.39	16.30
POTSC	13.54	2.230	83.15	25.10

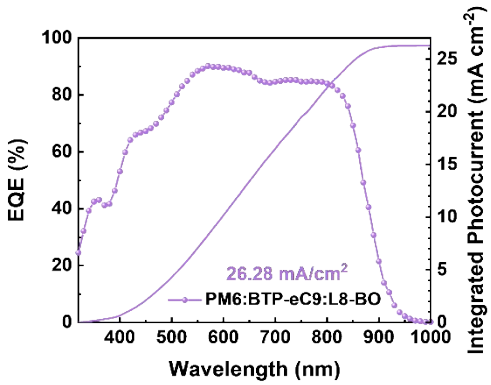

Figure S31. EQE spectra of PM6:BTP-eC9:L8-BO-based OSCs.

Table S10. Photovoltaic parameters and hysteresis index of POTSCs with 2PACz and 2PACz-K.

Condition	Scan Direction	J_{sc} (mA cm^{-2})	V_{OC} (V)	*FF* (%)	PCE (%)	Hysteresis Index
2PACz	Reverse	13.56	2.125	80.52	23.20	0.0468
	Forward	12.70	2.132	78.98	21.39	
2PACz-K	Reverse	13.54	2.230	83.15	25.10	0.0371
	Forward	13.40	2.216	81.38	24.17	

Table S11. Summary of the reported V_{OC} and *FF* values of POTSCs.

V_{OC} (V)	Reference
2.230	This work
2.216	*Adv. Energy Mater.*, 2025, 2404092[S20]
2.210	*Nat. Commun.*, 2025, 16, 2759[S22]
2.197	*Adv. Mater.*, 2023, 36, 2306568[S24]
2.151	*Nat. Energy*, 2024, 9, 411[S27]
2.15	*Energy Environ. Sci.*, 2024, 17, 219[S23]
2.15	*Adv. Mater.*, 2023, 35, 2208604[S29]

2.15	*Nature*, 2022, 604, 280[S9]
2.147	*J. Mater. Chem. C*, 2025, 13, 6309[S26]
2.144	*Joule*, 2024, 8, 2554[S21]
2.14	*Adv. Mater.*, 2023, 35, 2305946[S25]
2.131	*Energy Environ. Sci.*, 2025, 18, 2536[S30]
2.120	*Nat. Energy*, 2024, 9, 592[S28]
2.12	*Adv. Funct. Mater.*, 2023, 33, 2308794[S31]
2.09	*Adv. Mater.*, 2023, 35, 2307502[S34]
2.063	*Nat. Energy*, 2022, 7, 229[S35]
2.05	*Adv. Funct. Mater.*, 2021, 32, 2109321[S36]
1.96	*Adv. Funct. Mater.*, 2022, 32, 2112126[S38]
1.953	*Nano Energy*, 2020, 78, 105238[S32]
1.902	*Joule*, 2020, 4, 1594[S39]
1.89	*J. Mater. Chem. A*, 2021, 9, 19778[S37]
1.88	*Adv. Mater.*, 2022, 34, 2108829[S33]
1.85	*Adv. Energy Mater.*, 2020, 10, 2000361[S40]
1.73	*Adv. Energy Mater.*, 2020, 10, 2001188[S41]

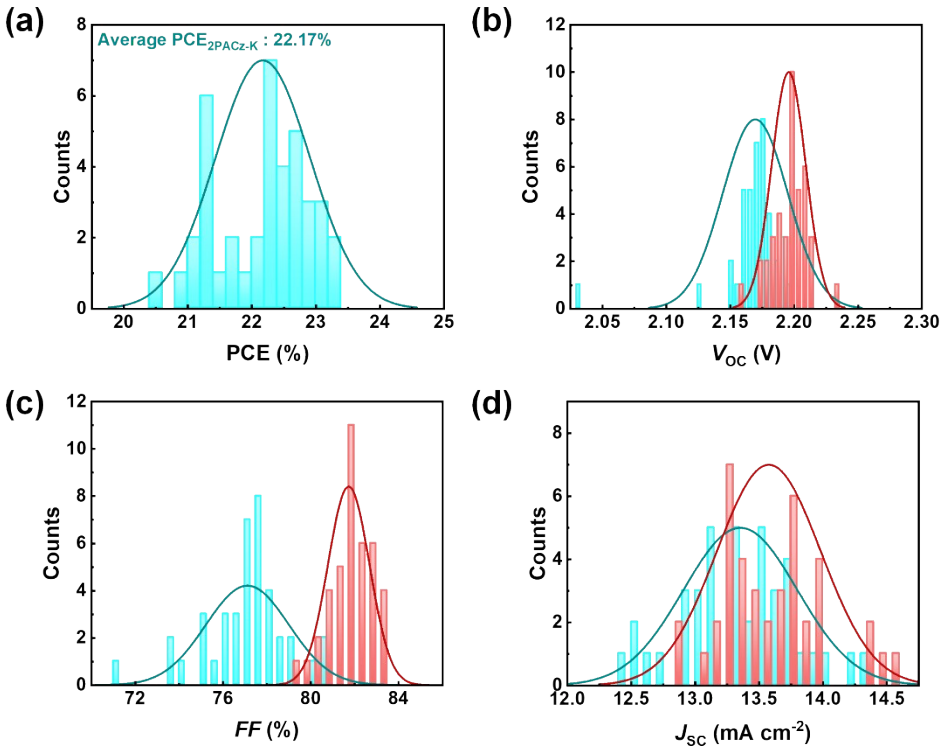

Figure S32. (a) PCE, (b) V_{OC}, (c) *FF*, and (d) J_{SC} distribution histogram of POTSCs with 2PACz and 2PACz-K.

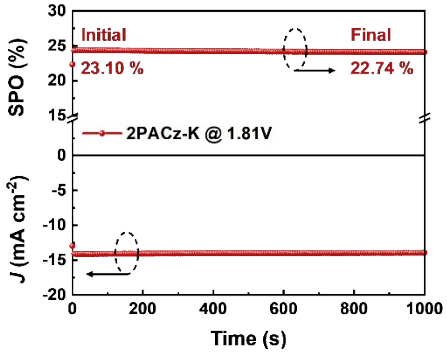

Figure S33. SPO tracking of POTSCs with 2PACz-K.

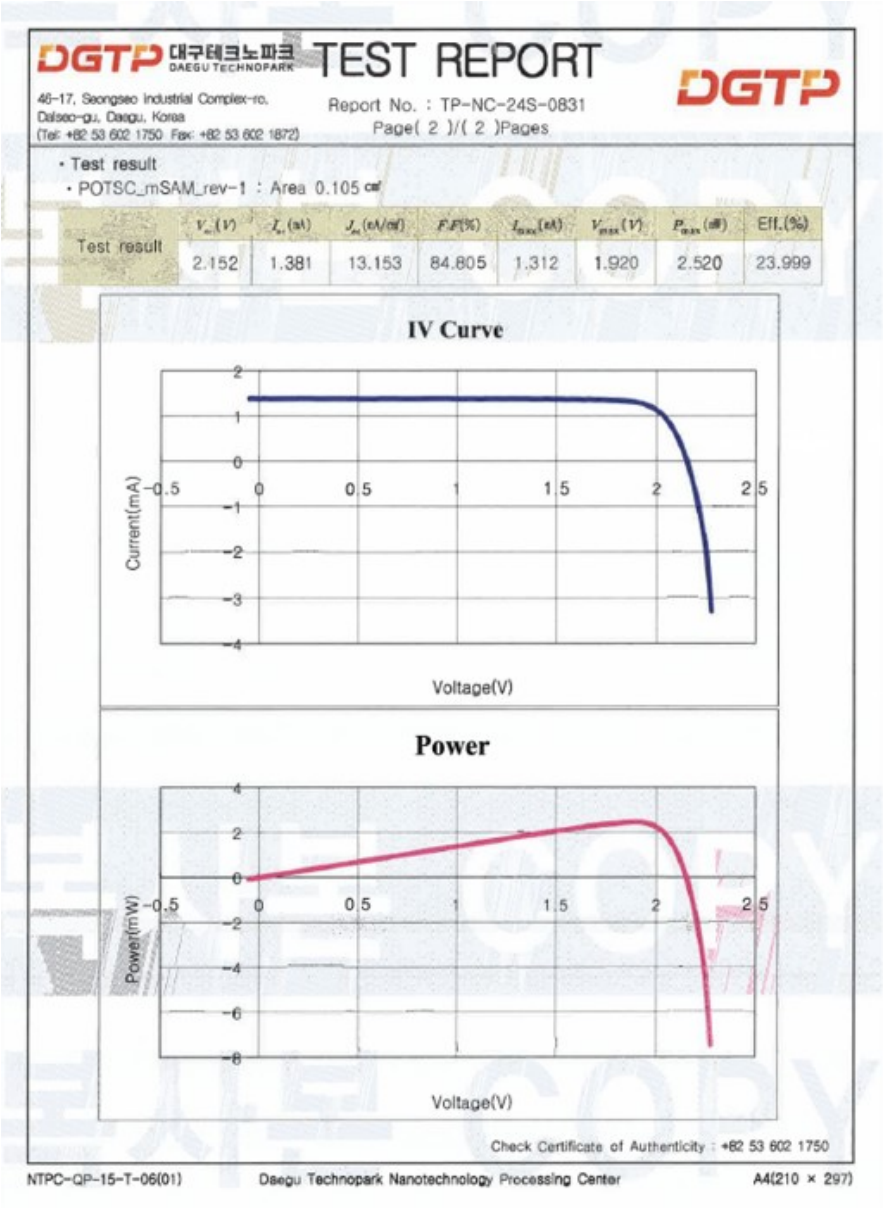

Figure S34. Certificate of 2PACz-K-based POTSC performance from the Korea Energy Agency (KEA), Daegu, South Korea.

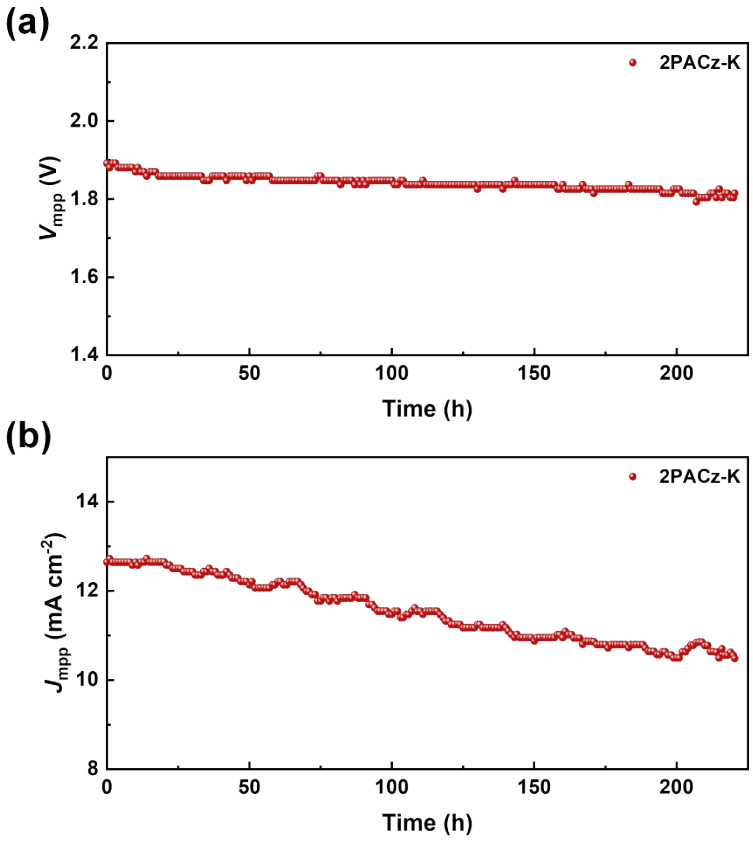

Figure S35. Operation stability of POTSCs at continuous output at MPP in ambient condition (25% RH, 40°C) under 100 mW cm^{-2}. (a) V_{mpp} and (b) J_{mpp}, respectively.

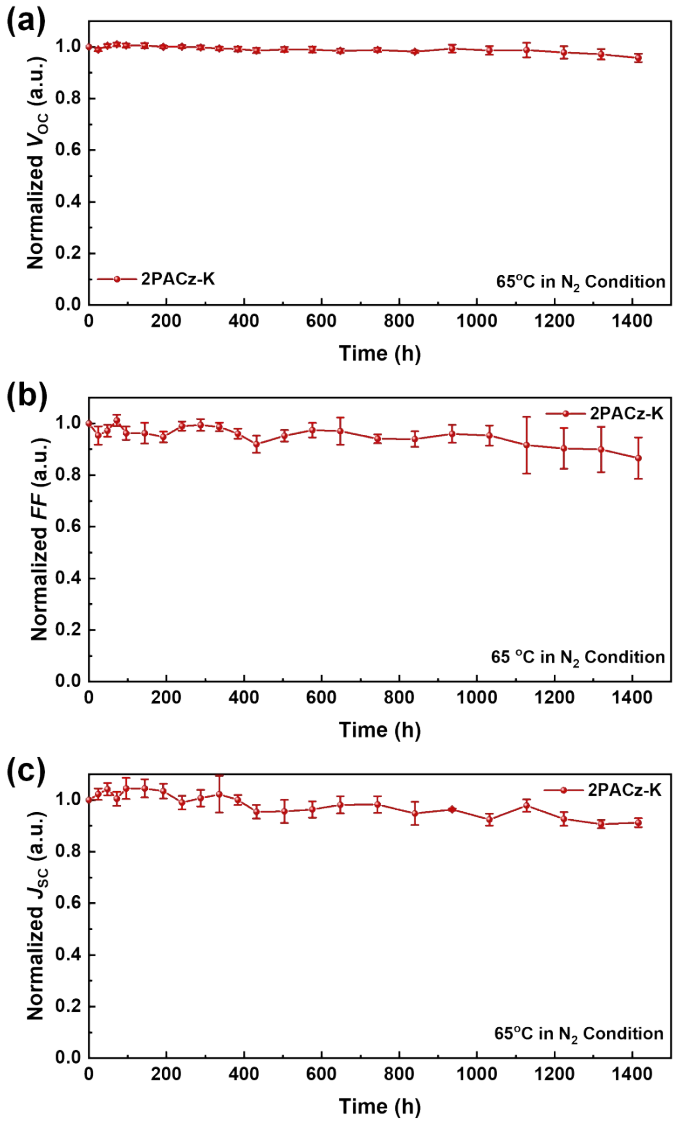

Figure S36. Thermal stability of POTSCs with 2PACz-K under 65°C in N_2 atmosphere. Normalized (a) V_{OC}, (b) *FF*, and (c) J_{SC}, respectively.

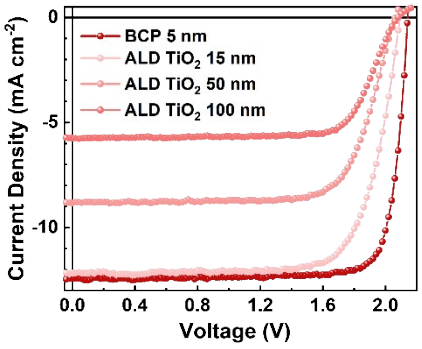

Figure S37. *J-V* curves of champion POTSCs with BCP and varying thickness of ALD TiO_x (without MgF_2 antireflection layer).

Table S12. Photovoltaic parameters of champion POTSCs with BCP and varying thickness of ALD TiO_x (without MgF_2 antireflection layer).

Condition	J_{SC} **(mA cm^{-2})**	V_{OC} **(V)**	***FF*** **(%)**	**PCE (%)**
BCP 5 nm	12.41	2.142	82.96	22.06
ALD TiO_x 15 nm (300 cycles)	12.16	2.093	74.74	19.02
ALD TiO_x 50 nm (1000 cycles)	8.34	2.087	72.13	12.55
ALD TiO_x 100 nm (2000 cycles)	5.75	2.079	75.63	9.04

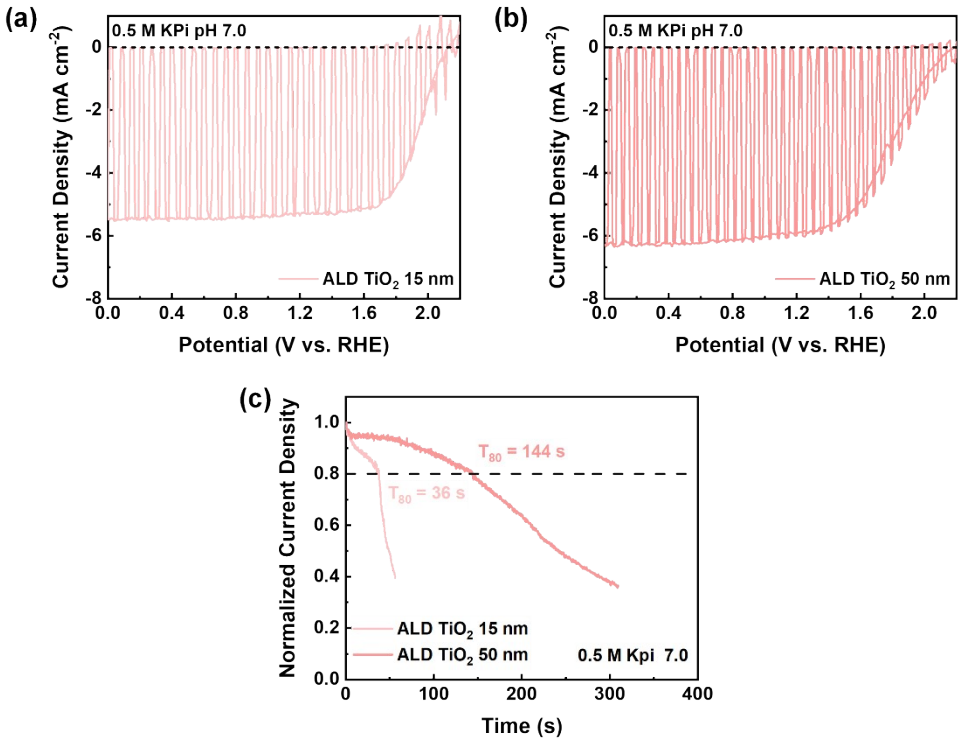

Figure S38. LSV curves of POTSC-PEC in 0.5 M KPi with (a) 18 and (b) 60 nm of ALD TiO_x. (c) CA measurement of POTSC-PEC at 0.1 V_{RHE} with 18 and 60 nm of ALD TiO_x

Supplemental References

S1. G. Kresse and J. Furthmuller, *Comp. Mater. Sci.*, 1996, **6**, 15–50.

S2. G. Kresse and J. Furthmüller, *Phy. Rev. B*, 1996, **54**, 11169–11186.

S3. J. P. Perdew, K. Burke and M. Ernzerhof, *Phys. Rev. Lett.*, 1996, **77**, 3865–3868.

S4. L. Wang, L. Yu, J.-Z. Wu, J. Wen and B.-S. Xiong, *Appl. Phys. Express*, 2019, **12**, 095002.

S5. P. Ágoston, P. Erhart, A. Klein and K. Albe, *J. Condens. Matter Phys.*, 2009, **21**, 455801.

S6. S. Kumari and P. Sautet, *J. Phys. Chem. Lett.*, 2023, **14**, 2635–2643.

S7. S. Grimme, A. Hansen, J. G. Brandenburg and C. Bannwarth, *Chem. Rev.*, 2016, **116**, 5105–5154.

S8. S. M. R. Islam, F. Khezeli, S. Ringe and C. Plaisance, *J. Chem. Phys.*, 2023, **159**.

S9. K. O. Brinkmann, T. Becker, F. Zimmermann, C. Kreusel, T. Gahlmann, M. Theisen, T. Haeger, S. Olthof, C. Tuckmantel, M. Gunster, T. Maschwitz, F. Gobelsmann, C. Koch, D. Hertel, P. Caprioglio, F. Pena-Camargo, L. Perdigon-Toro, A. Al-Ashouri, L. Merten, A. Hinderhofer, L. Gomell, S. Zhang, F. Schreiber, S. Albrecht, K. Meerholz, D. Neher, M. Stolterfoht and T. Riedl, *Nature*, 2022, **604**, 280–286.

S10. X. Y. Chin, D. Turkay, J. A. Steele, S. Tabean, S. Eswara, M. Mensi, P. Fiala, C. M. Wolff, A. Paracchino, K. Artuk, D. Jacobs, Q. Guesnay, F. Sahli, G. Andreatta, M. Boccard, Q. Jeangros and C. Ballif, *Science*, 2023, **381**, 59–63.

S11. J. Liu, Y. He, L. Ding, H. Zhang, Q. Li, L. Jia, J. Yu, T. W. Lau, M. Li, Y. Qin, X. Gu, F. Zhang, Q. Li, Y. Yang, S. Zhao, X. Wu, J. Liu, T. Liu, Y. Gao, Y. Wang, X. Dong, H. Chen, P. Li, T. Zhou, M. Yang, X. Ru, F. Peng, S. Yin, M. Qu, D. Zhao, Z. Zhao, M. Li, P. Guo, H. Yan, C. Xiao, P. Xiao, J. Yin, X. Zhang, Z. Li, B. He and X. Xu, *Nature*, 2024, **635**, 596–603.

S12. A. M. K. Fehr, A. Agrawal, F. Mandani, C. L. Conrad, Q. Jiang, S. Y. Park, O. Alley, B. Li, S. Sidhik, I. Metcalf, C. Botello, J. L. Young, J. Even, J. C. Blancon, T. G. Deutsch, K. Zhu, S. Albrecht, F. M. Toma, M. Wong and A. D. Mohite, *Nat. Commun.*, 2023, **14**, 3797.

S13. R. Lin, H. Gao, J. Lou, J. Xu, M. Yin, P. Wu, C. Liu, Y. Guo, E. Wang, S. Yang, R. Liu, D. Zhou, C. Ding, A. D. Bui, N. Yin, D. H. Macdonald, C.-Q. Ma, Q. Chen, K. Xiao, X. Luo, Y. Liu, L. Li, Y. Li, C. Chang and H. Tan, *Nature*, 2025, **648**, 600–606.

S14. Z. Liu, R. Lin, M. Wei, M. Yin, P. Wu, M. Li, L. Li, Y. Wang, G. Chen, V. Carnevali, L. Agosta, V. Slama, N. Lempesis, Z. Wang, M. Wang, Y. Deng, H. Luo, H. Gao, U. Rothlisberger, S. M. Zakeeruddin, X. Luo, Y. Liu, M. Grätzel and H. Tan, *Nat. Mater.*, 2025, **24**, 252–259.

S15. Z. Song, C. Li, L. Chen, K. Dolia, S. Fu, N. Sun, Y. Li, K. Wyatt, J. L. Young, T. G. Deutsch and Y. Yan, *ACS Energy Lett.*, 2023, **8**, 2611–2619.

S16. X. Jiang, S. Qin, L. Meng, G. He, J. Zhang, Y. Wang, Y. Zhu, T. Zou, Y. Gong, Z. Chen, G. Sun, M. Liu, X. Li, F. Lang and Y. Li, *Nature*, 2024, **635**, 860–866.

S17. Y. Han, J. Fu, Z. Ren, J. Yu, Q. Liang, Z. Xu, X. Xie, D. Li, R. Ma, M. Cao, Y. Sun,

C. Yang, J. He, X. Chang, K. Liu, P. W. K. Fong, J. Huang, H. Liu, Z. Liu, D. Xu, L. Cheng, J. Zhang, G. Yang, X. Lu, Y. Zhu, Q. Tai, Q. Lin, H. Hu, Y. Yang and G. Li, *Nat. Energy*, 2025, **10**, 513–525.

S18. C. Li, Y. Chen, Y. Li, L. Gong, Z. Yuan, L. Liang, J. Chen, P. Ganesan, Y. Zhang, J. Ma and P. Gao, *Angew. Chem., Int. Ed.*, 2025, **64**, e202420585.

S19. J. Yang, W. Sheng, X. Li, Y. Zhong, Y. Su, L. Tan and Y. Chen, *Adv. Funct. Mater.*, 2023, **33**, 2214984.

S20. J. G. Son, S. Ameen, J. Roe, S. Park, J. Seo, J. Kim, A. B. Faheem, H.-e. Koo, S. O. Oh, Y. Jo, J. W. Kim, Y. Lee, Y. S. Shin, H. Jang, D. Lee, S. Hur, K.-K. Lee, S. Cho, D. S. Kim, J. Y. Kim and B. Kim, *Adv. Energy Mater.*, 2025, **15**, 2404092.

S21. X. Guo, Z. Jia, S. Liu, R. Guo, F. Jiang, Y. Shi, Z. Dong, R. Luo, Y.-D. Wang, Z. Shi, J. Li, J. Chen, L. K. Lee, P. Müller-Buschbaum, D. S. Ginger, D. J. Paterson and Y. Hou, *Joule*, 2024, **8**, 2554–2569.

S22. Y. An, N. Zhang, Q. Liu, W. Jiang, G. Du, D. Chen, M. Liu, X. Huang, T. Lei, Q. Qiu, F. R. Lin, X. C. Zeng, A. K. Y. Jen and H.-L. Yip, *Nat. Commun.*, 2025, **16**, 2759.

S23. S. Jiang, R. Wang, M. Li, R. Yu, F. Wang and Z. a. Tan, *Energy Environ. Sci.*, 2024, **17**, 219–226.

S24. Y. An, N. Zhang, Z. Zeng, Y. Cai, W. Jiang, F. Qi, L. Ke, F. R. Lin, S.-W. Tsang, T. Shi, A. K.-Y. Jen and H.-L. Yip, *Adv. Mater.*, 2024, **36**, 2306568.

S25. X. Wang, D. Zhang, B. Liu, X. Wu, X. Jiang, S. Zhang, Y. Wang, D. Gao, L. Wang, H. Wang, Z. Huang, X. Xie, T. Chen, Z. Xiao, Q. He, S. Xiao, Z. Zhu and S. Yang, *Adv. Mater.*, 2023, **35**, 2305946.

S26. G. Xie, H. Li, J. Fang, X. Wang, L. Gan, N. Huang, H. Peng, X. Lin and L. Qiu, *J. Mater. Chem. C*, 2025, **13**, 6309–6318.

S27. S. Wu, Y. Yan, J. Yin, K. Jiang, F. Li, Z. Zeng, S.-W. Tsang and A. K. Y. Jen, *Nat. Energy*, 2024, **9**, 411–421.

S28. Z. Zhang, W. Chen, X. Jiang, J. Cao, H. Yang, H. Chen, F. Yang, Y. Shen, H. Yang, Q. Cheng, X. Chen, X. Tang, S. Kang, X.-m. Ou, C. J. Brabec, Y. Li and Y. Li, *Nat. Energy*, 2024, **9**, 592–601.

S29. H. Yang, W. Chen, Y. Yu, Y. Shen, H. Yang, X. Li, B. Zhang, H. Chen, Q. Cheng, Z. Zhang, W. Qin, J. D. Chen, J. X. Tang, Y. Li and Y. Li, *Adv. Mater.*, 2023, **35**, 2208604.

S30. X. Sun, F. Wang, G. Yang, X. Ding, J. Lv, Y. Sun, T. Wang, C. Gao, G. Zhang, W. Liu, X. Xu, S. Satapathi, X. Ouyang, A. Ng, L. Ye, M. Yuan, H. Zhang and H. Hu, *Energy Environ. Sci.*, 2025, **18**, 2536–2545.

S31. G. Xie, H. Li, X. Wang, J. Fang, D. Lin, D. Wang, S. Li, S. He and L. Qiu, *Adv. Funct. Mater.*, 2023, **33**, 2308794.

S32. S. Xie, R. Xia, Z. Chen, J. Tian, L. Yan, M. Ren, Z. Li, G. Zhang, Q. Xue, H.-L. Yip and Y. Cao, *Nano Energy*, 2020, **78**, 105238.

S33. S. Qin, C. Lu, Z. Jia, Y. Wang, S. Li, W. Lai, P. Shi, R. Wang, C. Zhu, J. Du, J. Zhang, L. Meng and Y. Li, *Adv. Mater.*, 2022, **34**, 2108829.

S34. Z. Ma, Y. Dong, R. Wang, Z. Xu, M. Li and Z. Tan, *Adv. Mater.*, 2023, **35**, 2307502.

S35. W. Chen, Y. Zhu, J. Xiu, G. Chen, H. Liang, S. Liu, H. Xue, E. Birgersson, J. W. Ho, X. Qin, J. Lin, R. Ma, T. Liu, Y. He, A. M.-C. Ng, X. Guo, Z. He, H. Yan, A. B. Djurišić and Y. Hou, *Nat. Energy*, 2022, **7**, 229–237.
S36. W. Chen, D. Li, X. Chen, H. Chen, S. Liu, H. Yang, X. Li, Y. Shen, X. Ou, Y. Yang, L. Jiang, Y. Li and Y. Li, *Adv. Funct. Mater.*, 2022, **32**, 2109321.
S37. X. Wu, Y. Liu, F. Qi, F. Lin, H. Fu, K. Jiang, S. Wu, L. Bi, D. Wang, F. Xu, A. K. Y. Jen and Z. Zhu, *J. Mater. Chem. A*, 2021, **9**, 19778–19787.
S38. Y. M. Xie, Q. Yao, Z. Zeng, Q. Xue, T. Niu, R. Xia, Y. Cheng, F. Lin, S. W. Tsang, A. K. Y. Jen, H. L. Yip and Y. Cao, *Adv. Funct. Mater.*, 2022, **32**, 2112126.
S39. X. Chen, Z. Jia, Z. Chen, T. Jiang, L. Bai, F. Tao, J. Chen, X. Chen, T. Liu, X. Xu, C. Yang, W. Shen, W. E. I. Sha, H. Zhu and Y. Yang, *Joule*, 2020, **4**, 1594–1606.
S40. Z. Li, S. Wu, J. Zhang, K. C. Lee, H. Lei, F. Lin, Z. Wang, Z. Zhu and A. K. Y. Jen, *Adv. Energy Mater.*, 2020, **10**, 2000361.
S41. H. Aqoma, I. F. Imran, F. T. A. Wibowo, N. V. Krishna, W. Lee, A. K. Sarker, D. Y. Ryu and S.-Y. Jang, *Adv. Energy Mater.*, 2020, **10**, 2001188.